Calculation And Design Of Power Split Device On A Hybrid Vehicle

Tran Thanh An, Duong Quang Minh, and Nguyen Van Tuan*

Faculty of Mechanical Engineering, University of Transport Technology, No. 54 Trieu Khuc Street, Thanh Xuan District, Hanoi 100000, Vietnam

Corresponding author. E-mail: nguyenvantuan@utt.edu.vn

Received: May 29, 2023; Accepted: September 22, 2023

Hybrid car technology is a combination of the advantages of pure electric cars and fossil fuel cars. Due to the electric motor (EM) support, the internal combustion engine (ICE) does not have to work in inefficient areas, saving fuel and reducing environmental pollution. However, to distribute the right source of motivation and the working mode, the role of the coordinator is vital. This paper aims to calculate the combination of two power sources from the EM and the ICE on hybrid cars. After calculating the design, the calculation and strength test of the power combiner was carried out using Ansys software. Results of this study showed that the maximum stress on the ring gear, sun gear, planetary gear, and the shaft is 160.89 Mpa, 175.56 Mpa, 239.03 Mpa, and 415.56 Mpa, respectively, and the maximum deformation on the ring gear, sun gear, planetary gear, and the shaft is 0.0104 mm, 0.017 mm, 0.0184 mm, and 0.178 mm, respectively. This shows that the article's results can be used in research on the Power Split Device in Hybrid cars.

Keywords: Hybrid Car; Power Split Device; Internal Combustion Engine; Electric Motor

http://dx.doi.org/10.6180/jase.202406_27(6).0005

1. Introduction

Today, the environment is a particular issue that is always a concern both within a country and worldwide. Pollution caused by motor vehicles is a problem for countries. One of the solutions to reduce environmental pollution is to use electric cars; in the future, electric car experts will be the primary means and the main object of the intelligent transport system [1–3]. Hybrid cars (HEV) are considered one of the most promising solutions to environmental degradation and the shortage of petroleum resources from the transportation industry [4]. Thanks to two power sources (thermo-electricity), hybrid cars can be adapted to work according to different operating conditions to achieve high efficiency and energy efficiency [5–7]. This efficient operation is due to the power split device. Therefore, if the power divider of this system is not studied, calculated, and controlled correctly during the mode conversion, it will easily cause a significant reduction in vehicle speed, increase fuel consumption, and cut off power in severe cases [8].

Hybrid car technology combines the advantages of pure electric vehicles and fuel-powered vehicles, and at the same time, it can achieve fuel savings rates of 15%-50% [9, 10]. Moreover, some scientists have shown that HEV also dramatically reduces harmful components released into the environment. Therefore, HEV is very interested in environmental friendliness and fuel economy. Due to the support of the electric motor, the heat engine does not have to work in inefficient areas, thereby saving fuel and reducing environmental pollution [11, 12]. However, to distribute the power source correctly and in the working mode, the role of the power combiner is vital. The power divider used in hybrid cars often uses the speed differential type; the studies on calculating the power split device are as follows:

In one study, Jinming Liu et al. [13] presented a design process that allows systematic search and screening through all three main aspects of Hybrid car design - sys-

tem configuration, and controls- to achieve optimal performance while meeting the imposed constraints. An automated dynamic modeling method was developed for the first time to enable the efficient modeling of hybrid vehicles. Of the 288 kinetically viable configurations, 17 were found to be driveable by a small electric motor. Only two models are suitable for power division at high speeds.

In another study, Xiaowu Zhang et al. [14] analyzed all possible configurations of hybrid powertrains using planetary gear dividers. The analysis shows there can be 12 different configurations, of which 6 are input split and 6 are output split. The authors have focused on two Toyota Prius and Chevy Volt designs. Dynamic programming solutions show that, in general, having more operating modes improves fuel economy because those additional modes give more flexibility to the parts of the powertrain to work efficiently.

In addition, the study [15] presented a dynamic model of the Toyota Hybrid powertrain. This hybrid system contains a planetary gear system to power split devices, combining the benefits of series and parallel hybrid vehicles. The authors used the Toyota Hybrid system model to apply model controller development. Two control algorithms are used: the dynamic stochastic programming method and the equivalent consumption minimization strategy. Both control strategies are near-optimal, demonstrating good fuel economy when tested under driving cycles.

Through the analysis of the above studies, the power divider plays a vital role for hybrid cars in switching modes by different operating conditions. On the other hand, the power divider also plays the role of helping to control the electric motor to follow the internal combustion engine by the operating requirements. This paper presents a method to build the relationship between torque, electric motor speed, internal combustion engine speed, and output torque. Then, the authors applied Ansys software to calculate and test the durability of the components in the power split device.

2. Selection of a power combiner for hybrid cars

2.1. Hybrid drivetrain analysis and differential selection

There are three types of transmission on hybrid cars: serial hybrid drive, parallel hybrid drive, and mixed hybrid drive. When the car is operating in the city, the EM will drive the vehicle; When the car is working in the suburbs, the ICE will cause the vehicle; when the car is operating on the highway, both EM and ICE work to drive the vehicle. This hybrid system has a component called a "Power split device" that continuously transforms the power of the EM and ICE to the active wheels of the car. This drive system is schematically shown in Figure 1. The author will study the power divider used for this hybrid transmission in this study.

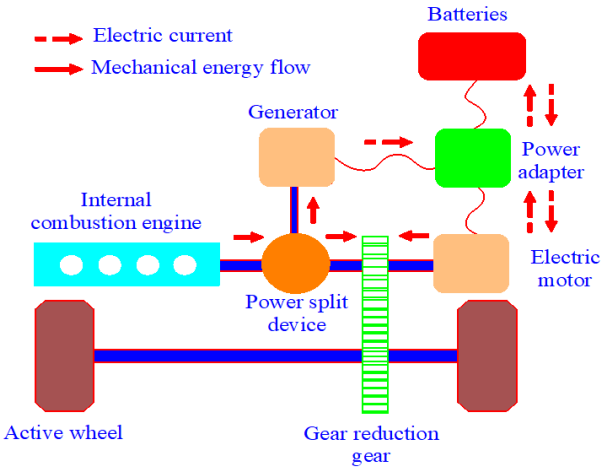

Fig. 1. Hybrid transmission diagram.

2.2. Build each speed and torque relationship of the driving forces in the combiner

The transmission diagram using the speed differential power divider is shown in Figure 2. The power split device used in this study is the speed differential type demonstrated in Figure 2.a, consisting of the sun gear, ring gear, planetary gear, and arm.

The ring gear is driven from the power source B through a pair of reduction gears Z_b, Z_a. The power combiner also has locks K_1, K_2, and collet (1) mounted on body (2).

2.2.1. *When motion combines both dynamic sources A and B*

Where: M_1 is source torque A transmitted to central gear;

M_2 : B source torque transmitted to ring gear;

The transmission diagram in Figure 2.a operates when both power sources A and B are active, then clutch L_1 and L_2 are in the closed state; locks K_1 and K_2 are open.

- Speed relationship:

We need to determine the relationship between the angular speeds ω_1, ω_2, and ω_3, which is the angular speed of the arm C ($\omega_3 = \omega_c$). In relative motion concerning lever C, the gear ratio between gear (1) and gear (2) is single:

$$i_{12}^{C} = \frac{\omega_1 - \omega_C}{\omega_2 - \omega_C} \tag{1}$$

On the other hand, there are: $i_{12}^{C} = \frac{-R_2}{R_1}$

Since ($\omega_3 = \omega_c$), we infer:

$$\omega_1 + \omega_2 \frac{R_2}{R_1} = \omega_3 \left(1 + \frac{R_2}{R_1}\right) \tag{2}$$

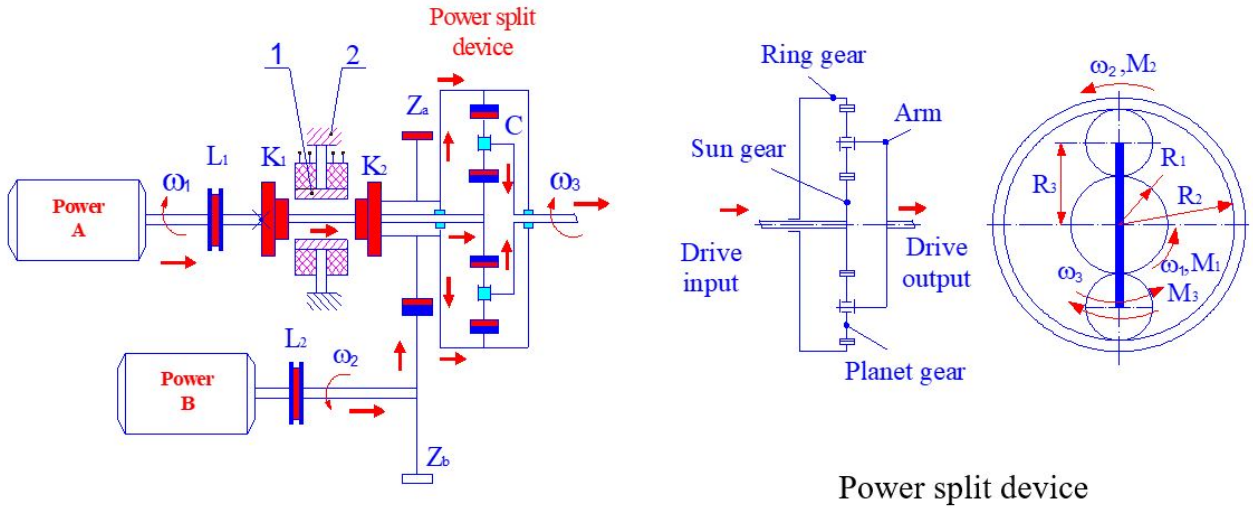

(a) The transmission diagram has both power sources A and B working together.

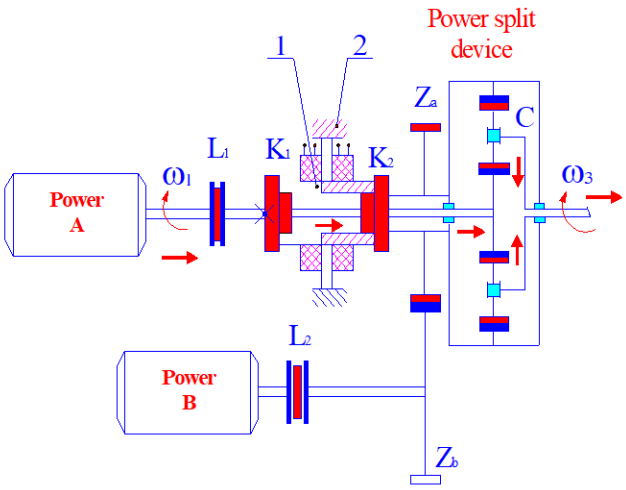

(b) Drive diagram with only power A active.

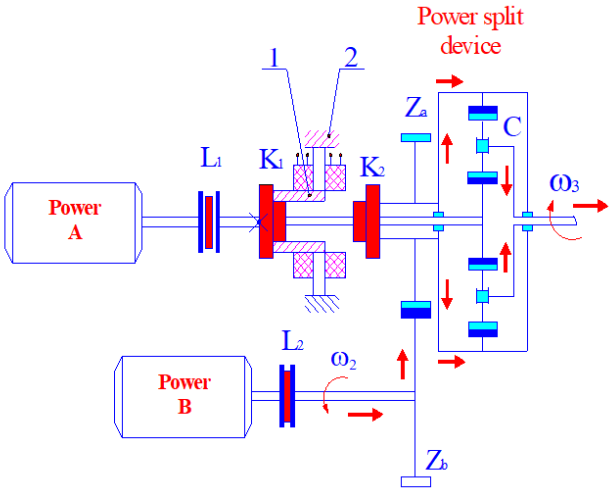

(c) Drive diagram with only power B active.

Fig. 2. Transmission diagram using a speed differential power split device. 1- Clamps 2- Shell K_1, K_2 - Electromagnetic lock R_1- Sun gear split ring radius R_2- Radius of the ring gear ring R_3- Radius of the circle through the shaft centers of the planetary gears ω_1- Angle speed of the source A ω_2- Angular momentum of source B and gear Z_a ($Z_a = Z_b$) ω_3- Output angular momentum of the power combiner L_1, L_2- The corresponding clutches source A, source B

Infer:

$$(R_1 + R_2) = 2R_3 \tag{3}$$

Instead, we have

$$\omega_3 = \frac{R_1}{2R_3}\omega_1 + \frac{R_2}{2R_3}\omega_2 \tag{4}$$

- Moment relationship:

According to the structure of the power combiner, gears (1) and (2) are the two top links (input shaft of the power combiner) that produce the torques M_1 and M_2. The Clever is the lead (output shaft of the power combiner).

Let $M_3{}^*$ be the proper resistance torque acting on the lever C

Applying, we have the equation of change of kinetic energy:

$$M_1.\omega_1 + M_2.\omega_2 + M_3{}^*.\omega_3 = 0 \tag{5}$$

Applying, we have the equation of change of angular momentum:

$$M_3{}^* = -(M_1 + M_2) \tag{6}$$

Substituting in the moment expression, we get:

$$\frac{M_2}{M_1} = -\frac{\omega_1 - \omega_C}{\omega_2 - \omega_C} = -i_{12}^C = \frac{R_2}{R_1} \tag{7}$$

Inferred:

$$M_3^* = -\frac{2R_3}{R_1} \cdot M_1 = -\frac{2R_3}{R_2} \cdot M_2 \tag{8}$$

We know the output shaft torque of the power combiner, so

$$M_3 = \frac{2R_3}{R_1} \cdot M_1 = \frac{2R_3}{R_2} \cdot M_2 \quad (9)$$

2.2.2. *When there is only source of motivation A*

The transmission diagram in Figure 2.b works when power source A is active and power source B is inactive when clutch L_1 is closed; Clutch L_2 is open; Lock K_1 is open, Lock K_2 is closed. Regarding the speed relation, from expression (4), when the ring gear speed $\omega_2 = 0$

We have:

$$\omega_3 = \frac{R_1}{2R_3}\omega_1 \quad (10)$$

Therefore, the torque at the output shaft of the combiner has the value:

$$M_3 = \frac{2R_3}{R_1}M_1 \quad (11)$$

2.2.3. *When only transmitting motivation B*

The transmission diagram in Figure 2.c operates when power source B is active, and power source A is inactive when clutch L_1 is in the open state; Clutch L_2 is in the closed state; Lock K_1 is closed; Lock K_2 is open. Regarding the speed relationship, from the speed relation expression (4), when the speed of the hub gear $\omega_1 = 0$, we have:

$$\omega_3 = \frac{R_2}{2R_3}\omega_2 \quad (12)$$

Therefore, the torque at the output shaft of the combiner has the value:

$$M_3 = \frac{2R_3}{R_2}M_2 \quad (13)$$

From the dynamic relations presented above, the speed differential power divider has the advantage of ensuring speed flexibility from two combined driving dynamics sources. The power combiner output shaft is connected from the independent speeds (completely independent of each other) of the two power sources, so it is very convenient to design to operate in a wide speed range.

3. Calculation and design of power split device

3.1. Calculating the number of teeth in the power split device

After analyzing the transmission diagrams to arrange the power source, the author found that the power split device diagram, as shown in Figure 3, is suitable for the study.

The output power source is provided by the input power source and is related to the latter by their speed and torque. The power split device has a diagram, as shown in Figure 3, including three gates and 2 degrees of freedom. Gate

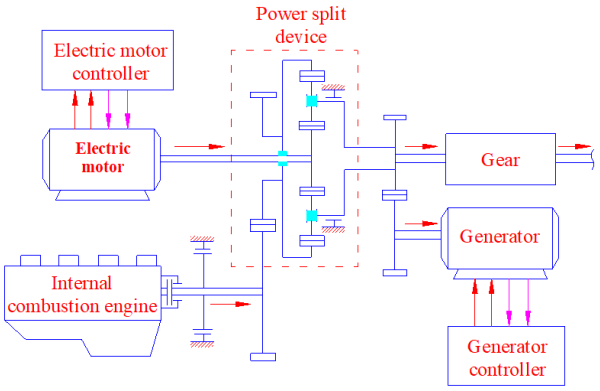

Fig. 3. Diagram of the power split device in a hybrid system.

1 connects to ICE; Gate 2 connects to EM with unidirectional energy flow. Gate 3 can be connected to the end transmission with bidirectional energy flow.

From the power split device diagram, as shown in Figure 4, the input shaft from ICE is connected to the sun gear, the input shaft from EM is connected to the guide arm of the planetary gear, and the ring gear is connected to the primary beam of the gearbox.

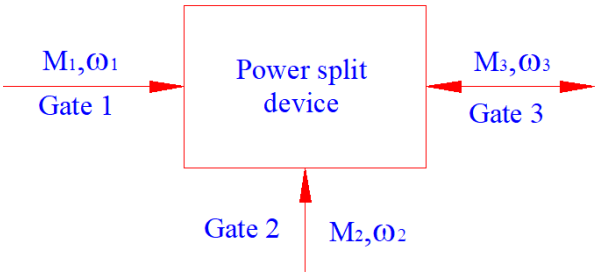

Fig. 4. Power combiner diagram.

The input port parameters are:

Electric motor: $M_1 = 50(\text{Nm})$, $\omega_1 = 4000(\text{rpm})$.

Heat engine: $M_2 = 90.32(\text{Nm}), \omega_2 = 6400(\text{rpm})$. In hybrid mode, there is a torque relationship between the two inputs $M_1/k_1 = M_2/k_2$ and output speed $\omega_3 = k_1\omega_1 + k_2\omega_2$.

According to Willets's formula, we have $\omega_3 = k_1\omega_1 + k_2\omega_2$.

$$\begin{cases} \frac{M_1}{k_1} = \frac{M_2}{k_2} = \frac{M_1+M_2}{k_1+k_2} \\ k_1 + k_2 = 1 \\ M_1 = 50(N.m) \\ M_1 = 90.32(N.m) \end{cases} \Rightarrow \begin{cases} k_1 = 0.356 \\ k_2 = 0.644 \end{cases}$$

Calculation of tooth ratio ratios between gear pairs in base transmission We have: $k_1 = \frac{R_1}{2R_3}$; $k_2 = \frac{R_2}{2R_3}$

$$\begin{cases} k_1 = 0.356 \\ k_2 = 0.644 \end{cases} \quad Z = \frac{R_2}{R_1} = \frac{0.644}{0.356} = 1.809$$

3.2. Designing parameters of gears

Normal modulus: $m_n = 2(\text{ mm})$

Tooth pitch: $t = \pi \cdot m_n = 3.14 * 2 = 6.28(\text{ mm})$

The tilt angle of teeth: $\beta = 30^\circ$

Number of sun gear teeth: $Z_R = 54$ (teeth)

Number of planetary gear teeth: $Z_p = 12$ (teeth)

Number of sun gear teeth: $Z_s = 30$ (teeth)

- Ring gear:

Table 1. Specifications of gear ring.

No	Name	Value	Unit
1	Normal Module (m)	2	mm
2	Tilt angle of teeth (β)	30^0	degree
3	Diameter of dividing ring (d_R)	124.71	mm
4	Diameter of crown ring (d_{aR})	120.71	mm
5	Diameter of tooth base ring (d_{fR})	129.71	mm
6	Gear thickness	25	mm

- Sun gear:

Table 2. Sun gear parameters.

No	Name	Value	Unit
1	Normal Module (m)	2	mm
2	Tilt angle of teeth (β)	30^0	degree
3	Diameter of dividing ring (d_R)	69.28	mm
4	Diameter of crown ring (d_{aR})	73.28	mm
5	Diameter of tooth base ring (d_{fR})	64.28	mm
6	Gear thickness	25	mm

- Planetary gear:

Table 3. Planetary gear parameters.

No	Name	Value	Unit
1	Normal Module (m)	2	mm
2	Tilt angle of teeth (β)	30°	degree
3	Diameter of dividing ring (d_f)	27.71	mm
4	Diameter of crown ring (d_{aR})	31.71	mm
5	Diameter of tooth base ring (d_{fR})	22.71	mm
6	Gear thickness	25	mm

From the data in Table 1, Table 2 and Table 3, we can build a power split device, as shown in Figure 5.

3.3. Building a model and calculating the power distribution test

3.3.1. *Determine the force acting on the gears*

The Willson planetary set's force analysis diagram is shown in Figure 6: from the graph of Figure 6 on the planetary gear, the forces acting in opposite directions are the radial force F_r and the axial force F_a. Since the basic geometry of the whole Wilson transmission is the same, the forces acting on the planetary gear are of the same magnitude.

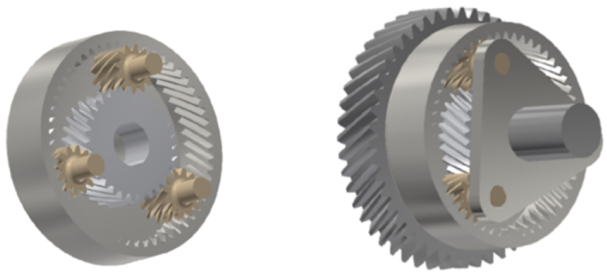

Fig. 5. Power split device.

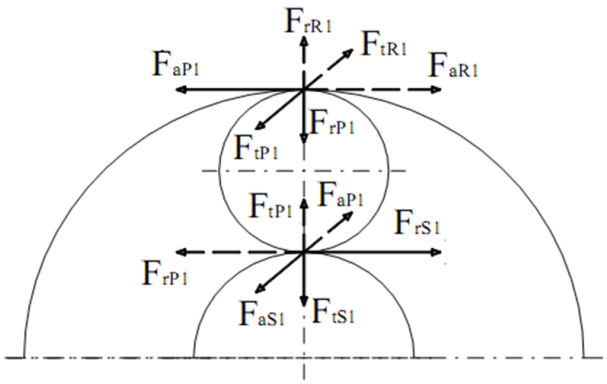

Fig. 6. Force diagram on the Wilson transmission.

+ Ring force

Ring force acting on the front planetary gear set:

$$P_R = \frac{2 \cdot M_{ti}}{3 \cdot d_i} = \frac{M_1}{3 \cdot d_R} = \frac{2 * 90.32.10^3}{3 * 124.71} = 482.82(N)$$

We have: $P_p = P_S = P_R = 482,82(\text{ N})$

+ Centripetal force

$$F_{ri} = 482.82^* \frac{\text{tg}\,20^\circ}{\cos 30^\circ} = 202.92(\text{ N})$$

+ Axial force

$$F_{ai} = P_{i.} \cdot \text{tg}\,\beta = 482.82 * \text{tg}\,30^\circ = 278.76(\text{ N})$$

3.3.2. *Choose material*

We chose the same gear material because the gears can be used through maintenance, overhaul, and repair cycles and are convenient for mass production. However, the gears have the same module, so when the gears engage, the large gears will bear less load, so when the small gear has to be overhauled, the big gear is still usable. We choose 40CrNi alloy steel, Large gear: I improve HRC $= 55 \div 63$; Allowable overload stress $[\sigma_H]_{max} = 1960(\text{MPa})$; $[\sigma_F]_{1\,max} = 560(\text{MPa})$; $[\sigma_F]_{2\,max} = 560(\text{MPa})$

Due to the characteristics of the vehicle designed with constantly changing operating modes, high-speed movement, and unstable load, the shaft material is 20CrNi

steel. HRC hardness from 46 ÷ 53; Endurance limit σ_b = 1000(MPa); The yield strength σ_{ch} = 750 (MPa).

3.3.3. *The sequence of calculating the combiner on Ansys software*

The differential actuator model was estimated and tested by ANSYS Workbench 19.2 software.

The software simulates the following steps:

- 3D shapes of various part shapes and their assemblies modelled using Inventor design software;

- Planetary gear assemblies exported from Inventor in IGES format and imported in ANSYS Workbench Program (ANSYS 19.2);

- Select the appropriate type of analysis: Static structural analysis;

- Definition of the static boundary condition of high school: The ring is fixed;

- Determination of material properties; here, all gear and transport materials are standard steel: Only Modulus of Elasticity, Poison Ratio, and Density are required; - Load assignment for static simulation: Torque acting on the shaft;

- Define contact patterns to determine how contact surfaces can move relative to each other.

The power divider conducts meshing after being imported into ANSYS software, as shown in Figure 7.

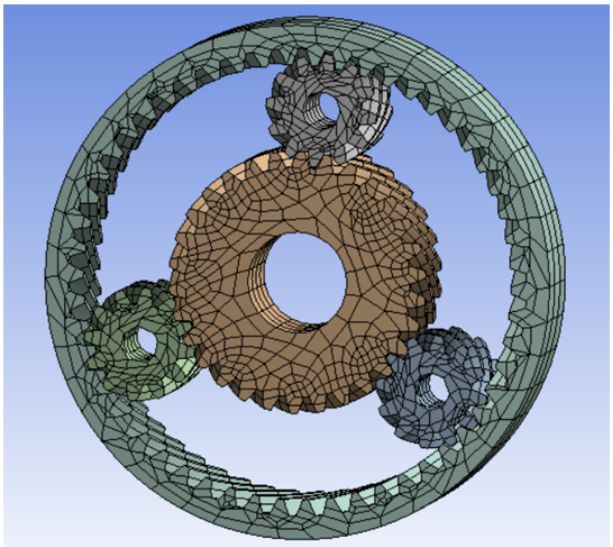

Fig. 7. Power combiner drawing and meshing.

4. Results and discussion

When the car operates on the highway, the power combiner bears the most significant load so the author will calculate and test the combiner in this mode.

4.1. Ring gear

The tooth of the ring is subject to bending and wear; the part where it bears the maximum force is the tooth root. It is considered that there are three teeth in contact with the planetary gear. Tangential force (F_t) due to the torque transmitted by the equipment on these three teeth. The tangential force is distributed among the three teeth, with one tooth-bearing 50% of the force and the other paying 25% of each tooth. Another force acting on the gear is the radial force (F_r) generated by the separation force between the two meshing gears. This force acts on the centre of the equipment. The magnitudes of the forces (F_t) and (F_r) working on the bag are taken from the above design values. The most significant stress areas mainly appear at the surface of the teeth of the ring gear, as shown in Figure 8 (the red area in Figure). The maximum stress value generated on the ring gear is 160.89 MPa. On the other hand, the most significant displacement of the ring gear is shown as shown in Figure 9, with a maximum displacement value of 0.0104 mm. The causes of stress and large displacement at these positions are the maximum bearing teeth. But, these values still ensure safety for the ring gear. The stress distribution on this Ring gear is similar to that shown in the study [16].

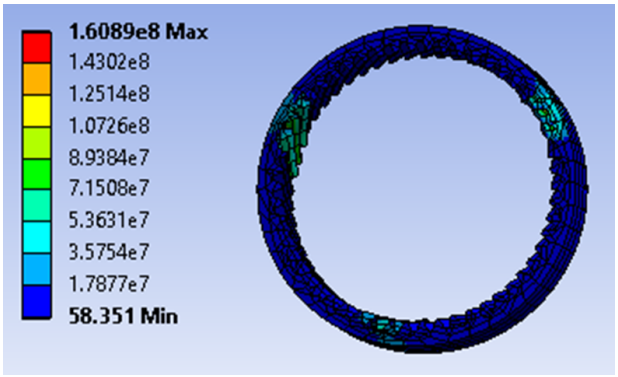

Fig. 8. Stress analysis of gear rings in Ansys.

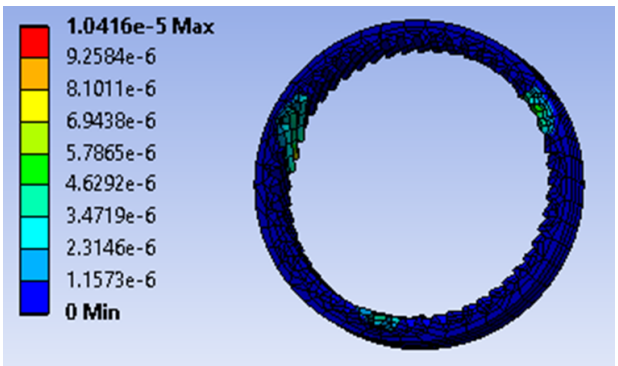

Fig. 9. Maximum deformation of the Ansys gear ring.

4.2. Sun gear

When designing sun gear, the gear has three forces. These are the radial force (F_r), tangential force (F_t), and axial force (F_a). These three forces were applied to the gear teeth to analyze the force acting on the spur gear. They are considered to have six teeth that mesh with the sun gear. The stress results are shown in Figure 10, and the deformation results are shown in Figure 11. Similarly, at the exposure surfaces of the maximum bearing teeth, the maximum stress value generated in gear is 175.56 MPa, and the maximum deformation is 0.017 mm. These values still ensure the safety of gears. The stress distribution on this gear has the same rule as shown in the study [17].

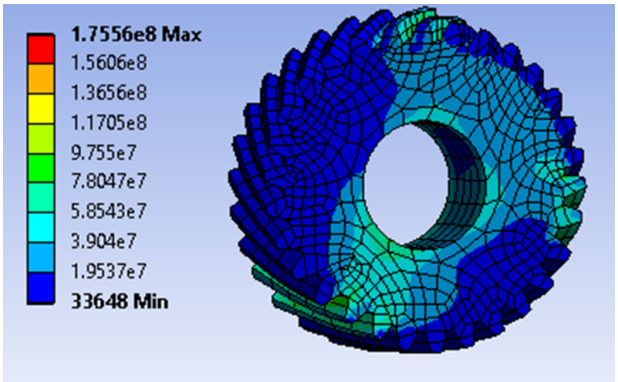

Fig. 10. Stress analysis of sun gears in Ansys.

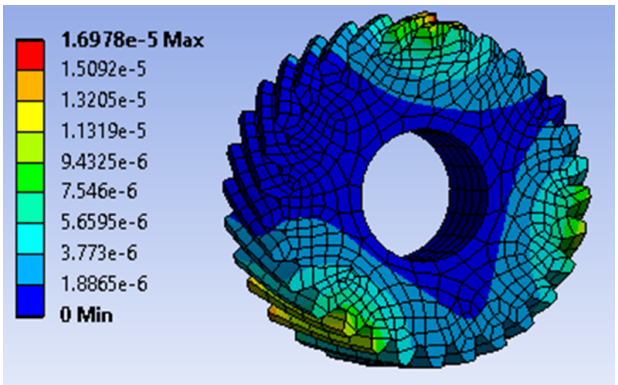

Fig. 11. Maximum distortion of sun gear in Ansys.

4.3. Planetary gears

The planetary gear is mounted on the cross pin and drives the sun gear when the differential works. It is constrained on the inner cylinder face and the forces acting on the two teeth. These forces are calculated by considering the two teeth in contact with the sun gear. We see that the most significant stress occurs at the tooth root of the planetary gear.

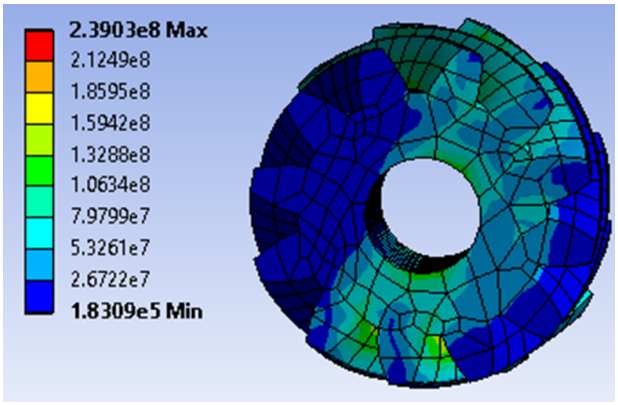

Fig. 12. Stress analysis of planetary gears in Ansys.

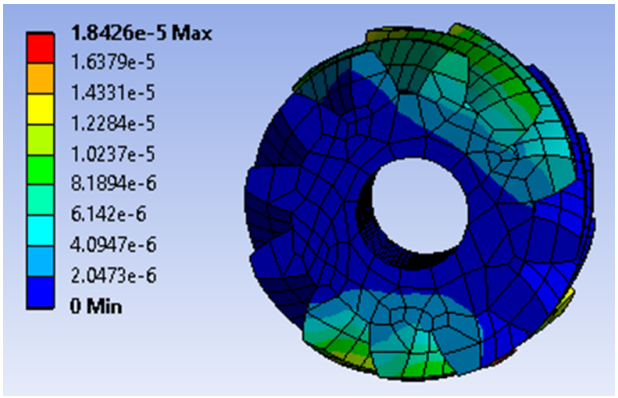

Fig. 13. Maximum deformation of planetary gears in Ansys.

The stress results are shown in Figure 12, and the deformation results are shown in Figure 13. We see that the maximum stress appears on the contact surfaces of the planet gear. Similarly, at the contact surfaces of the maximum bearing teeth, the highest stress value is 239.03 MPa, and the maximum hammock in this section is 0.0184 mm. These values still ensure the safety of gears. The stress distribution on this gear has the same rule as shown in the study [17].

4.4. Link shaft

The shaft includes the sun gear shaft and the shaft that links the three planetary gears together. The small head is connected to the gears. The larger end of the pin is supported on bearings mounted inside the sun gear. Compression is applied to the end face of the plug, and all other faces are fixed. This compression force is calculated from the radial force on the ring gear. The stress results are shown in Figure 14, and the deformation results in Figure 15. The shaft with the sun gear has a maximum stress of 415.56 MPa, and the maximum deformation of the post is 0.178

mm; this value is within safe limits.

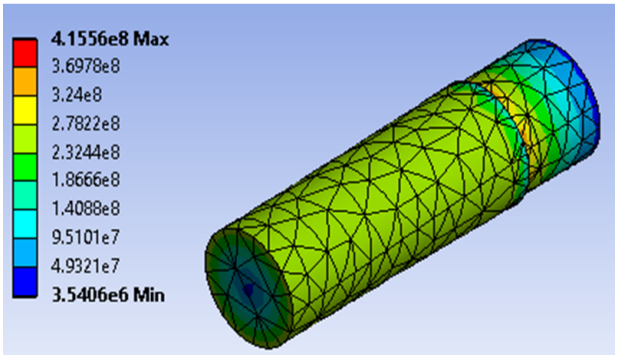

Fig. 14. Sun gear shaft stress analysis in Ansys.

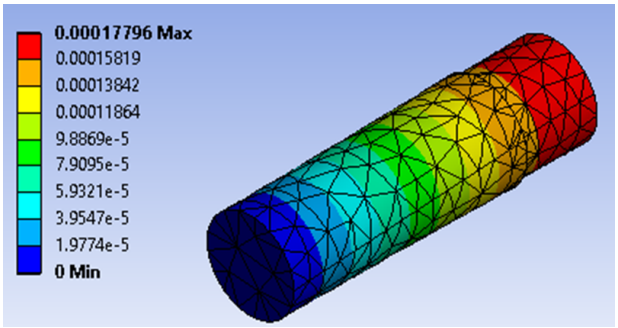

Fig. 15. Maximum deformation of sun gear shaft in Ansys.

5. Conclusions

Based on the selected differential power split, each speed and torque relationship of the input and output power sources were built in three modes: mode when there is a combination of both motivational sources A and B; when only motivation source A is active; when only motivation source B is active.

In this study, Ansys software was used to calculate and test the power combiner with the maximum stress generated on the gear ring of 160.89 MPa and the maximum strain of 0.0104 mm; the maximum stress induced in the sun gear is 175.56 MPa, and the maximum strain is 0.017 mm; the maximum stress generated in the planetary gear is 239.03 MPa and the maximum strain is 0.0184 mm; the maximum stress and maximum displacement occurring on the sun gear shaft are 415.56 MPa and 0.178 mm. The resulting stresses and strains are within the allowable range to avoid load and fatigue failure.

Finally, a power split device design calculation method combined with endurance test calculation on Ansys software has been proposed. Using this method will provide more accuracy and reliability than the traditional method and easily change the structure adjustment without spending much time recalculating from the beginning. On the other hand, the proposed method can be used to study hybrid automobile systems and design and manufacture power split devices.

References

[1] S.-Y. Chen, C.-H. Wu, Y.-H. Hung, and C.-T. Chung, (2018) *"Optimal strategies of energy management integrated with transmission control for a hybrid electric vehicle using dynamic particle swarm optimization"* **Energy *160***: 154–170. DOI: 10.1016/j.energy.2018.06.023.

[2] D. Mohanraj, J. Gopalakrishnan, B. Chokkalingam, and L. Mihet-Popa, (2022) *"Critical Aspects of Electric Motor Drive Controllers and Mitigation of Torque Ripple-Review"* **IEEE Access**: DOI: 10.1109/ACCESS.2022.3187515.

[3] M. Deepak, G. Janaki, C. Bharatiraja, et al., (2022) *"Design Switched Reluctance Motor Rotor Modification Towards Torque Ripple Analysis For EVs"* **Journal of Applied Science and Engineering *26***(7): 949–958. DOI: 10.6180/jase.202307_26(7).0006.

[4] Z. Song, X. Zhang, J. Li, H. Hofmann, M. Ouyang, and J. Du, (2018) *"Component sizing optimization of plug-in hybrid electric vehicles with the hybrid energy storage system"* **Energy *144***: 393–403. DOI: 10.1016/j.energy.2017.12.009.

[5] J. Zhang, T. Shen, and J. Kako, (2019) *"Short-term optimal energy management of power-split hybrid electric vehicles under velocity tracking control"* **IEEE Transactions on Vehicular Technology *69***(1): 182–193. DOI: 10.1109/TVT.2019.2950042.

[6] X. Zeng and J. Wang, (2015) *"A parallel hybrid electric vehicle energy management strategy using stochastic model predictive control with road grade preview"* **IEEE Transactions on Control Systems Technology *23***(6): 2416–2423. DOI: 10.1109/TCST.2015.2409235.

[7] S. Xie, H. He, and J. Peng, (2017) *"An energy management strategy based on stochastic model predictive control for plug-in hybrid electric buses"* **Applied energy *196***: 279–288. DOI: 10.1016/j.apenergy.2016.12.112.

[8] A. Gao, Z. Fu, and F. Tao, (2020) *"Dynamic coordinated control based on sliding mode controller during mode switching with ICE starting for an HEV"* **IEEE Access *8***: 60428–60443. DOI: 10.1109/ACCESS.2020.2983613.

[9] M. A. Hannan, F. Azidin, and A. Mohamed, (2014) *"Hybrid electric vehicles and their challenges: A review"* **Renewable and Sustainable Energy Reviews *29***: 135–150. DOI: 10.1016/j.rser.2013.08.097.

[10] B. Liu, L. Li, X. Wang, and S. Cheng, (2018) *"Hybrid electric vehicle downshifting strategy based on stochastic dynamic programming during regenerative braking process"* **IEEE Transactions on Vehicular Technology *67***(6): 4716–4727. DOI: 10.1109/TVT.2018.2815518.

[11] B. V. Padmarajan, A. McGordon, and P. A. Jennings, (2015) *"Blended rule-based energy management for PHEV: System structure and strategy"* **IEEE Transactions on Vehicular Technology *65***(10): 8757–8762. DOI: 10.1109/TVT.2015.2504510.

[12] J. Peng, H. Fan, H. He, and D. Pan, (2015) *"A rule-based energy management strategy for a plug-in hybrid school bus based on a controller area network bus"* **Energies *8***(6): 5122–5142.

[13] J. Liu and H. Peng, (2010) *"A systematic design approach for two planetary gear split hybrid vehicles"* **Vehicle System Dynamics *48***(11): 1395–1412.

[14] C.-T. Li, X. Zhang, and H. Peng. "Design of power-split hybrid vehicles with a single planetary gear". In: *Dynamic systems and control conference*. ***45301***. American Society of Mechanical Engineers. 2012, 857–865. DOI: 10.1109/TVT.2012.2208210.

[15] J. Liu and H. Peng, (2008) *"Modeling and control of a power-split hybrid vehicle"* **IEEE transactions on control systems technology *16***(6): 1242–1251. DOI: 10.1109/TCST.2008.919447.

[16] A. Kawalec, J. Wiktor, and D. Ceglarek, (2006) *"Comparative analysis of tooth-root strength using ISO and AGMA standards in spur and helical gears with FEM-based verification"* ***128***(5): 1141–1158. DOI: 10.1115/1.2214735.

[17] M. Murali and S. A. Prasad, (2016) *"Influence of module and pressure angle on contact stresses in spur gears"* ***5***(3): 224–228. DOI: 10.18178/ijmerr.5.3.224-228.